Cell Reports
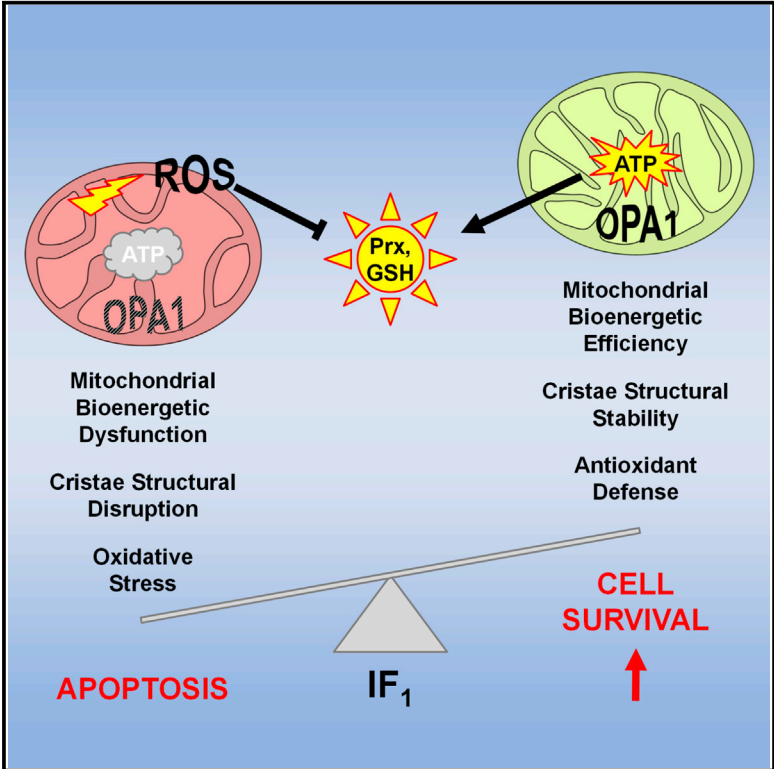
Control of Mitochondrial Remodeling by the ATPase Inhibitory Factor 1 Unveils a Pro-survival Relay via OPA1

Graphical Abstract

Authors

Danilo Faccenda, Junji Nakamura, Giulia Gorini, Gurtej K. Dhoot, Mauro Piacentini, Masusuke Yoshida, Michelangelo Campanella

Correspondence

mcampanella@rvc.ac.uk

In Brief

Mitochondrial dysfunction is linked to malignant growth and tumor resistance to chemotherapy. Faccenda et al. characterize the tumorigenic role of IF_1, which primes a pro-survival pathway by stabilizing OPA1 to hinder mitochondrial cristae remodeling during apoptosis.

Highlights

- Pro-oncogenic IF_1 maintains the mitochondrial ATP pool during apoptosis

- IF_1 promotes cancer cell survival by preventing GSH and Prx3 inactivation

- IF_1 inhibits OMA1-mediated processing of OPA1, impeding apoptotic cristae remodeling

- Anti-apoptotic role of IF_1 is linked to both mitochondrial metabolism and structure

CrossMark

CellPress

Control of Mitochondrial Remodeling
by the ATPase Inhibitory Factor 1 Unveils
a Pro-survival Relay via OPA1

Danilo Faccenda,[1,2] Junji Nakamura,[3] Giulia Gorini,[1] Gurtej K. Dhoot,[1] Mauro Piacentini,[2,4] Masusuke Yoshida,[3]
and Michelangelo Campanella[1,2,5,*]
[1]Department of Comparative Biomedical Sciences, The Royal Veterinary College London and UCL Consortium for Mitochondrial Research,
Royal College Street, NW1 0TU London, UK
[2]Department of Biology, University of Rome "Tor Vergata," 00133 Rome, Italy
[3]Kyoto Sangyo University, Kamigamo-Motoyama, Kyoto 603-8555, Japan
[4]National Institute for Infectious Diseases, IRCCS "Lazzaro Spallanzani," Rome, Italy
[5]Lead Contact
*Correspondence: mcampanella@rvc.ac.uk
http://dx.doi.org/10.1016/j.celrep.2017.01.070

SUMMARY

The ubiquitously expressed ATPase inhibitory factor 1 (IF_1) is a mitochondrial protein that blocks the reversal of the F_1F_o-ATPsynthase, preventing dissipation of cellular ATP and ischemic damage. IF_1 suppresses programmed cell death, enhancing tumor invasion and chemoresistance, and is expressed in various types of human cancers. In this study, we examined its effect on mitochondrial redox balance and apoptotic cristae remodeling, finding that, by maintaining ATP levels, IF_1 reduces glutathione (GSH) consumption and inactivation of peroxiredoxin 3 (Prx3) during apoptosis. This correlates with inhibition of metallopeptidase OMA1-mediated processing of the pro-fusion dynamin-related protein optic atrophy 1 (OPA1). Stabilization of OPA1 impedes cristae remodeling and completion of apoptosis. Taken together, these data suggest that IF_1 acts on both mitochondrial bioenergetics and structure, is involved in mitochondrial signaling in tumor cells, and may underlie their proliferative capacity.

INTRODUCTION

Cancer is a complex disease that originates from the simultaneous deregulation of multiple signaling and metabolic pathways leading to uncontrolled cell growth and proliferation (Vogelstein and Kinzler, 1993; Seyfried et al., 2014). Despite the vast heterogeneity of genetic, epigenetic, and metabolic changes from which cancers arise, tumor cells share a series of common traits, known as the "hallmarks of cancer" (Hanahan and Weinberg, 2011). Among these is the ability to evade apoptosis and withstand both intracellular and extracellular death signals. Mitochondria are central regulators of apoptosis, during which they lose membrane integrity and release key proapoptotic factors (Tait and Green, 2010; Martinou and Youle,

2011). Mitochondria are dynamic organelles that fuse and divide to form a constantly changing network, which modulates mitochondrial metabolism (Benard and Rossignol, 2008; Westermann, 2012) and quality control (Twig and Shirihai, 2011; Ni et al., 2015).

Proteins involved in the control of mitochondrial dynamics also regulate apoptosis (Otera and Mihara, 2012). During apoptosis, tubular mitochondria fragment into small isolated puncta (Frank et al., 2001), the tightly packed lamellar cristae swell and mitochondrial inner membrane (MIM) organization is lost (Scorrano et al., 2002). Apoptotic mitochondrial remodeling is mainly sustained by recruitment of the pro-fission factor dynamin-related protein 1 (Drp1) and proteolytic cleavage of the structural protein optic atrophy 1 (OPA1).

The ATPase inhibitory factor 1 (IF_1), which is upregulated in many human carcinomas (Sánchez-Cenizo et al., 2010; Song et al., 2014; Yin et al., 2015), is implicated in the control of both mitochondrial bioenergetics and structure, by regulating the activity and oligomerization of the F_1F_o-ATPsynthase (hereinafter referred to as ATP synthase) (García et al., 2006; Campanella et al., 2008). Furthermore, the level of IF_1 expression in hepatocellular carcinomas, gliomas, and gastric cancers correlates with aggressiveness and invasiveness of tumors and poor prognosis in patients (Song et al., 2014; Yin et al., 2015; Wu et al., 2015). We previously demonstrated that IF_1 promotes cell survival against apoptosis by blocking mitochondrial remodeling (Faccenda et al., 2013b).This associates with counteraction of Bax and Drp1 recruitment, hindering mitochondrial fission, permeabilization, and cytochrome c (cyt c) release, which are key events of intrinsic apoptosis (Galluzzi et al., 2015).

Cristae morphogenesis and structure are regulated by the synergetic activity of OPA1 and the ATP synthase. While OPA1 oligomers guarantee formation and closure of the cristae junctions, dimers of ATP synthase drive the invagination of the MIM and form ribbons at the cristae tips that maintain their curvature (Davies et al., 2012; Daum et al., 2013). Interestingly, by binding to the ATP synthase, IF_1 not only inhibits its hydrolytic activity, but also stabilizes its dimerization (Tomasetig et al.,
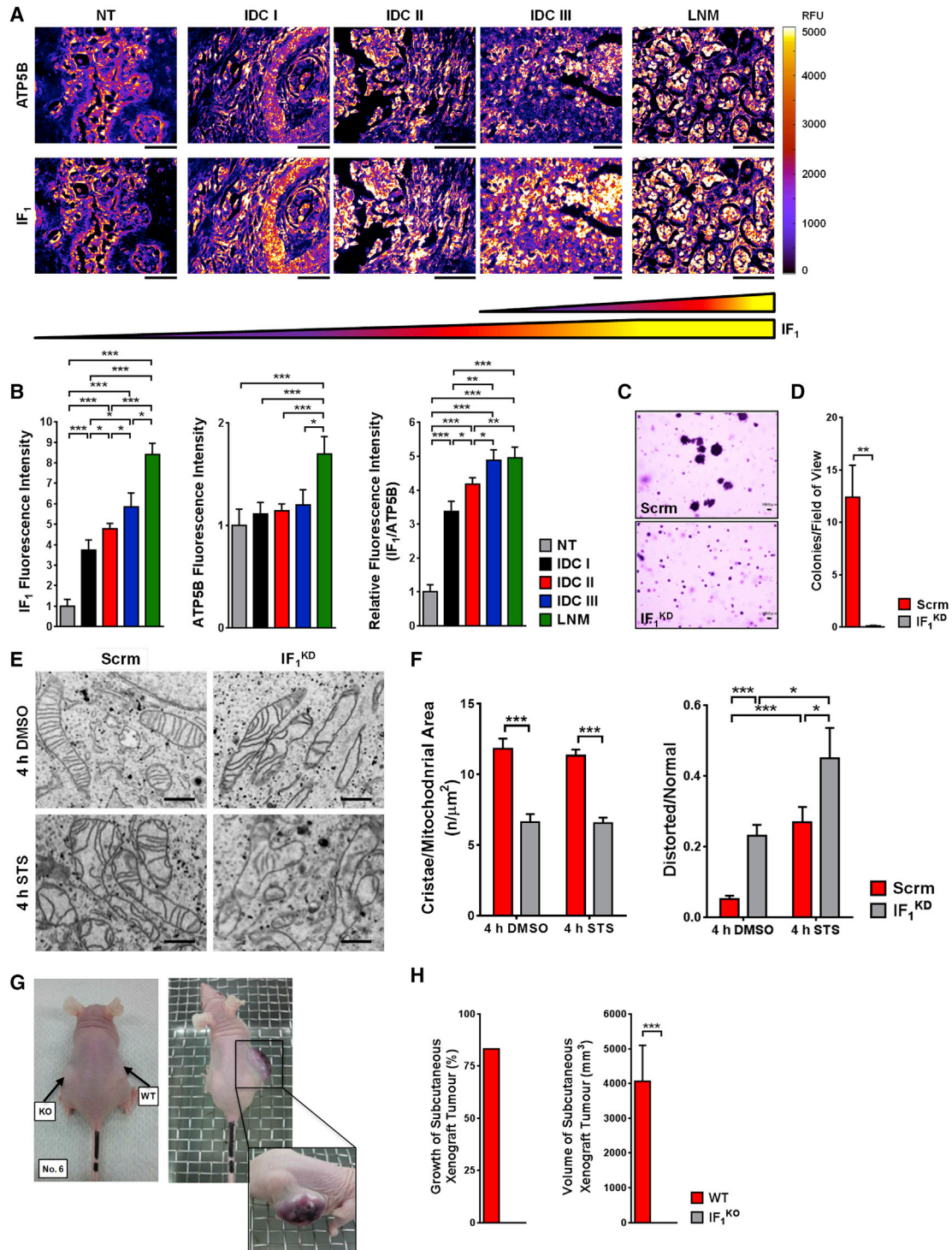
Figure 1. The Oncogenic Potential of IF$_1$

(A) Representative fluorescent IHC images of tissue sections of human breast IDC, from grade 1 to 3, and matched normal tissues (NT) and lymph node metastasis (LNM), immunostained for IF$_1$ and ATP5B. Images are presented as heatmaps, where the brightest pixels correspond to the areas of highest score (ranging from 0 to 5,000 relative fluorescence units [RFU]; scale bars, 100 μm).

(B) Bar charts of IF$_1$ (left) and ATP5B (middle) mean fluorescence intensities, and of IF$_1$:ATP5B fluorescence intensity ratio (right), in the different groups, normalized to grade 1. Data are presented as mean ± SEM; grade 1, n = 12; grade 2, n = 44; grade 3, n = 16, LNM, n = 36.

(C) Soft agar colony formation assay (scale bars, 100 μm).

(legend continued on next page)

2002; García et al., 2006). ATP hydrolysis induces a torque that pulls the ATP synthase monomers apart and facilitates the binding of IF$_1$, which then promotes formation of dimers and oligomers by blocking the counterclockwise rotation of the F$_1$ domain (Buzhynskyy et al., 2007).

Taking this evidence into account, we hypothesized that IF$_1$ can actively preserve the inner mitochondrial structure during apoptosis by regulating OPA1-mediated control of mitochondrial dynamics. This, together with the previously demonstrated regulation of Drp1 recruitment (Faccenda et al., 2013b), may be key to IF$_1$-mediated inhibition of cyt c release (Faccenda et al., 2013a).

Here, we show that during apoptosis OPA1 processing is prevented by IF$_1$ through functional interplay with the stress-activated protease OMA1 (Anand et al., 2014; Jiang et al., 2014). In parallel, IF$_1$ counteracts glutathione (GSH) loss and drives the ATP-dependent reactivation of the mitochondrial peroxidase peroxiredoxin 3 (Prx3), which promote cell survival under redox stress (Cunniff et al., 2014; Song et al., 2015). Consistent with previous findings, this work demonstrates that IF$_1$ counteracts the structural remodeling of mitochondria during apoptosis through concomitant regulation of both mitochondrial dynamics and metabolism.

RESULTS

The IF$_1$:ATP Synthase Expression Ratio Correlates with Tumor Grade and Oncogenic Potential

A positive correlation between IF$_1$ expression and cancer aggressiveness, via sustenance of the invasive and migratory phenotypes, has been recently proposed (Sánchez-Aragó et al., 2013; Song et al., 2014; Yin et al., 2015; Wu et al., 2015). Since malignancy-related changes in IF$_1$ levels relative to the ATP synthase may contribute to tumor progression, we analyzed whether the IF$_1$:ATP synthase ratio of expression varies according to tumor grade in invasive ductal carcinoma (IDC), the most common type of breast cancer. Breast carcinoma tissue microarrays (TMAs) with progressive changes were immunostained for IF$_1$ and the ATP synthase, β subunit (Figures 1A and S1). Interestingly, the IF$_1$:ATP synthase expression ratio increases accordingly to the degree of tumor dedifferentiation (Figure 1B). Our results corroborate previous findings (Song et al., 2014; Yin et al., 2015) and suggest a possible pro-tumorigenic metabolic impact through aberrant regulation of the ATP synthase.

In order to prove the oncogenic potential of IF$_1$, we then investigated the effect of IF$_1$ loss on the in vitro and in vivo proliferative capacity of cancer cells. By using stable knockdown (KD) HeLa cells (Fujikawa et al., 2012) (Figure S2A) and transformed IF$_1$ knockout (KO) mouse embryonic fibroblasts (MEFs) (Nakamura et al., 2013) (Figure S2B), we observed a drastic decrease in both anchorage-independent cell growth and xenograft tumor growth (Figures 1C, 1D, 1G, 1H, and S2C), highlighting IF$_1$ contribution to unregulated proliferation of cancer cells.

According to recent evidence, increased IF$_1$ levels confer a growth advantage to cancer cells by inducing structural and physiological alteration at the mitochondrial level (Sánchez-Aragó et al., 2012; Faccenda et al., 2013a). In particular, we showed that IF$_1$ expression level defines cell susceptibility to apoptosis (Faccenda et al., 2013b) by modulating mitochondrial structure (Campanella et al., 2008), thus affecting the inner membrane organization and retention of cyt c.

In order to provide further proof that alterations in the mitochondrial ultrastructure can be involved in IF$_1$-dependent tumorigenesis, we analyzed the topology of the MIM in IF$_1$ KD and control HeLa cells before and after induction of apoptosis (Figure 1E). Although no major changes in the organization of the cristae were previously highlighted (Fujikawa et al., 2012), at a closer examination we noticed that KD of IF$_1$ yielded cells with fewer mitochondrial cristae, which also appeared rather disorganized (Figure 1F). This confirms that IF$_1$ plays a part in the structural stability of mitochondrial membranes. Moreover, STS-induced cristae remodeling was more pronounced in IF$_1$ KD cells (Figure 1F). This effect most probably depends on the reduced level of mitochondrial inner membrane organization observed.

Interestingly, a substantial reduction in cristae number was recorded in liver mitochondria from IF$_1$ KO mice when compared to the wild-type (WT) line (Figure S2D). In contrast to previous examination (Nakamura et al., 2013), the TEM analysis described here revealed the presence of sizeable differences in mitochondrial morphology and ultrastructure between the two genetic backgrounds. We collected quantitative data by measuring the number of mitochondria in each cell and assessing their morphological differences, as well as comparing the density of mitochondrial cristae. Indeed, IF$_1$ ablation resulted in decreased number of mitochondria, accompanied by volume enlargement and cristae loss.

IF$_1$ Regulates Both Structure and Function of Mitochondria

Considering the effect of IF$_1$ on both mitochondrial structure and oncogenic potential of immortalized cells, we analyzed whether the pro-survival potential of the protein could be related to its inhibitory activity to ATP hydrolysis. For the purpose, we used two different mutant clones obtained by introducing missense mutations in the IF$_1$ cDNA (Figure 2A). IF$_1$^{E30A} carries a mutation in the inhibitory domain that impedes both binding to and regulation of the ATP synthase (Bason et al., 2011). In IF$_1$^{H49P}, pH-dependent regulation is affected instead, and the clone is active even in the basic physiological conditions of the mitochondrial matrix environment (similar to the H49K substitution [Cabezon et al., 2000; Sánchez-Cenizo et al., 2010]). Therefore,

(D) Column diagram reporting the average number of visible colonies (Ø > 100 μm). Data are presented as mean ± SEM; n = 4 (nine fields per dish).

(E) Representative TEM images of control and IF$_1$ KD HeLa cells at resting conditions and after treatment with STS (scale bars, 500 nm).

(F) Bar charts of mean cristae number per mitochondrial area (left) and ratio between distorted (horseshoe shaped, swollen, disorganized) and normal (lamellar and tubular) cristae (right), before and after treatment with STS. Data are presented as mean ± SEM; n = 3 (20 cells per grid).

(G) Xenograft analysis of nude mice inoculated with transformed WT and IF$_1$ KO MEFs.

(H) Column diagrams reporting the percentage of xenograft formation and the average xenograft size.
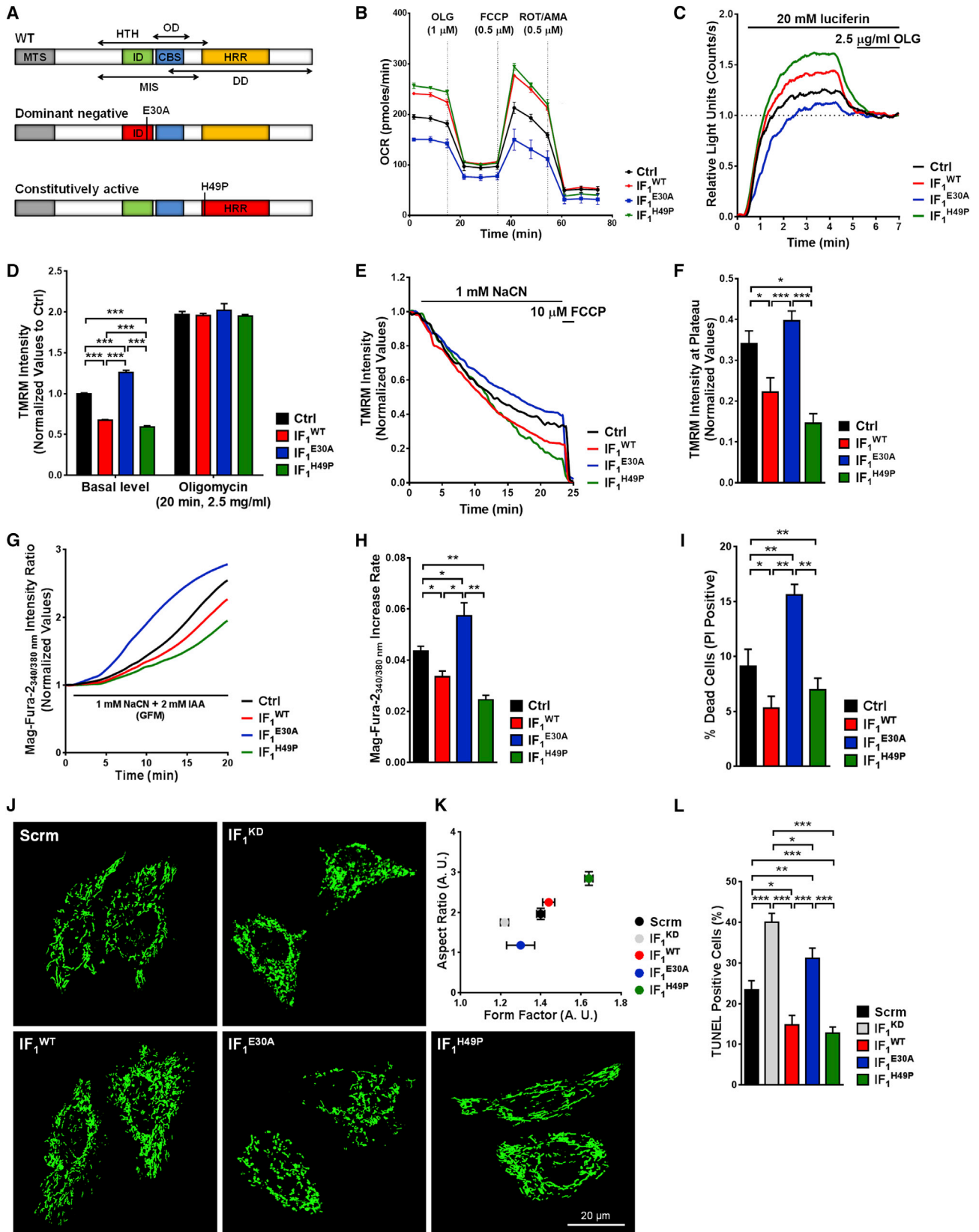
(legend on next page)

by complementing with endogenous IF$_1$, the two clones behave as dominant-negative (IF$_1^{E30A}$) and constitutively active (IF$_1^{H49P}$) mutants. We first monitored the levels of active dimers and inactive tetramers in transiently transfected HeLa cells (Figures S3A and S3B). As expected, IF$_1^{H49P}$ transfected cells were characterized by a higher IF$_1$ dimer:tetramer ratio, indicating an enhanced rate of dissociation of active dimers from inactive oligomers even at resting conditions.

Alteration in mitochondrial oxidative phosphorylation (OXPHOS) efficiency induced by the expression of the two IF$_1$ mutant clones was then determined by measuring changes in the oxygen consumption rate (OCR) and intracellular ATP levels in response to mitochondrial toxins. OCR was measured in untreated cells and upon challenge with oligomycin (OLG) to block ATP synthesis, carbonyl cyanide 4-trifluoromethoxy-phenylhydrazone (FCCP) to uncouple the MIM and a combination of rotenone (ROT), and antimycin A (AMA) to arrest mitochondrial respiration (Figure 2B). A luciferase assay was instead used to assess mitochondrial and cytosolic free ATP levels before and after addition of OLG (Figures 2C and S3E). Both assays revealed that mitochondrial bioenergetic efficiency is positively and negatively modulated by IF$_1^{H49P}$ and IF$_1^{E30A}$, respectively. In fact, the dominant-negative mutation (E30A) induced a decrease in the basal and maximal respiration rates (Figure S3C), which was paralleled by a reduction in the ATP synthase activity, as shown by its lower sensitivity to OLG (Figures S3D and S3F). IF$_1^{H49P}$, instead, had a greater effect on mitochondrial respiration and ATP synthesis than the WT protein, indicating that the two mutants are effectively able to modify the activity of endogenous IF$_1$ by complementation.

Further proof of the different behavior of the IF$_1$ mutant clones was obtained by measuring the mitochondrial membrane potential ($\Delta\Psi_m$) (Figure 2D). As widely reported, loss of IF$_1$ function produces an increase in $\Delta\Psi_m$ (Campanella et al., 2008; Barbato et al., 2015), which was observed in cells transfected with IF$_1^{E30A}$. IF$_1^{H49P}$ instead induced a significant decrease in basal $\Delta\Psi_m$. Subsequent incubation with OLG confirmed that these variations depend on interaction with the ATP synthase.

Finally, the inhibitory activities of the IF$_1$ mutant clones were evaluated by dynamically monitoring $\Delta\Psi_m$ and ATP levels in HeLa cells subjected to NaCN-induced ischemia (Figures 2E and 2G). The opposite responses to hypoxic-like conditions exhibited by HeLa cells expressing the two IF$_1$ mutant clones further demonstrated the effective modulation of endogenous IF$_1$ inhibitory activity (Figures 2F and 2H). Since inhibition of the ATP synthase reversal by IF$_1$ has a protective role against ischemic/hypoxic damage (Rouslin and Broge, 1996; Matic et al., 2016), we then tested whether cells transfected with the two mutant clones exhibit a different resistance to chemically induced ischemia. As shown in Figure 2I, cells expressing IF$_1^{E30A}$ were more susceptible than control cells to ischemia, while IF$_1^{H49P}$ was instead protective.

We then examined the impact on the mitochondrial network morphology by evaluating mitochondrial volume (profile area), length (aspect ratio, AR), and degree of branching (form factor, FF). Interestingly, both mutant clones affected these parameters producing opposite outcomes (Figures 2J and S3G). Indeed, IF$_1^{E30A}$ expressing HeLa cells were characterized by reduced mitochondrial volume and fragmentation of the mitochondrial network, while constitutive activation of IF$_1$ (IF$_1^{H49P}$) enhanced mitochondrial elongation and interconnectivity (Figures S3H and 2K). Furthermore, IF$_1$ KD HeLa showed comparable effects on AR and FF to the ones induced by IF$_1^{E30A}$ (Figure 2K). The result further corroborates the hypothesis that IF$_1$ has a physiological role in assisting the shaping of the mitochondrial internal structure and network morphology by binding the ATP synthase.

Figure 2. Regulation of Mitochondrial Function and Structure by IF$_1$ Clones

(A) Scheme of IF$_1$ and mutant clones structures. MTS, mitochondrial targeting sequence; ID, inhibitory domain; CBS, putative CaM-binding site; HRR, histidine-rich region.

(B) Representative graph of OCR in HeLa cells exposed to OLG (1 μM), FCCP (0.5 μM), and ROT/AMA (1 μM). Values were normalized to the mitochondrial protein content.

(C) Prototypical live-cell luciferase assay to measure basal intramitochondrial ATP levels. HeLa cells were transiently transfected with mitochondria-targeted luciferase (mLuc) and challenged with OLG (2.5 μg/mL).

(D) Bar chart showing differences in basal $\Delta\Psi_m$, measured with TMRM (30 nM), in HeLa cells expressing different IF$_1$ clones. Cells were co-transfected with yellow fluorescent protein (YFP) to allow for fluorescence-based selection, and imaged before and after exposure to OLG (2.5 μg/mL, 20 min).

(E) Prototypical traces of $\Delta\Psi_m$ loss in HeLa cells exposed to NaCN. Cells were co-transfected with YFP and the indicated construct, and loaded with TMRM (30 nM). TMRM emitted fluorescence was continuously monitored before and after addition of NaCN (1 mM). FCCP (20 nM) was added at plateau to confirm the directional behavior of the dye.

(F) Column diagram of mean TMRM intensity at plateau following NaCN treatment. Data are presented as mean $\pm$ SEM; n = 5 (seven to 12 cells per cover glass).

(G) Representative traces of Mag-Fura-2 fluorescence intensity in HeLa cells expressing WT and mutant IF$_1$. Cells, co-transfected with YFP, were challenged with 1 mM NaCN and 2 mM IAA, no glucose, to mimic ischemia-induced, ATP synthase reversal-driven depletion of cellular ATP. The subsequent increase in Mag-Fura-2$_{340/380\text{ nm}}$ intensity ratio, which reflects the rise in $[Mg^{2+}]_c$, was monitored as a readout of the degree of ATP synthase reversal.

(H) Bar chart of mean slopes of increase in Mag-Fura-2 intensity ratio, calculated via linearization, and fitting of raw traces. Data are presented as mean $\pm$ SEM; n = 4 (13–20 cells per cover glass).

(I) Histogram reporting percentage of propidium iodide (PI) positive HeLa cells transfected with different IF$_1$ mutant clones and subjected to chemical ischemia (2-hr incubation with 1 mM NaCN, 2 mM IAA, no glucose). Data are presented as mean $\pm$ SEM; n = 3 (>400 cells per cover glass).

(J) Representative images of mitochondrial network morphology in control HeLa cells, co-transfected with mitochondria-targeted green fluorescent protein (mtGFP) and the indicated constructs, and IF$_1$ KD cells expressing mtGFP.

(K) Scatterplot showing the analysis of mitochondrial AR and FF. Higher values (upper-right part of the diagram) indicate increased mitochondrial elongation and ramification. Data are presented as mean $\pm$ SEM; n = 3 (seven to 15 cells per cover glass).

(L) Average percentage of apoptosis in control HeLa cells expressing different IF$_1$ clones and IF$_1$ KD cells treated with STS. Cells were co-transfected with dsRed and the indicated construct and incubated with 1 μM STS for 12 hr. Apoptotic cells were stained with TUNEL assay. Data are presented as mean $\pm$ SEM; n = 4 (>500 cells per cover glass).
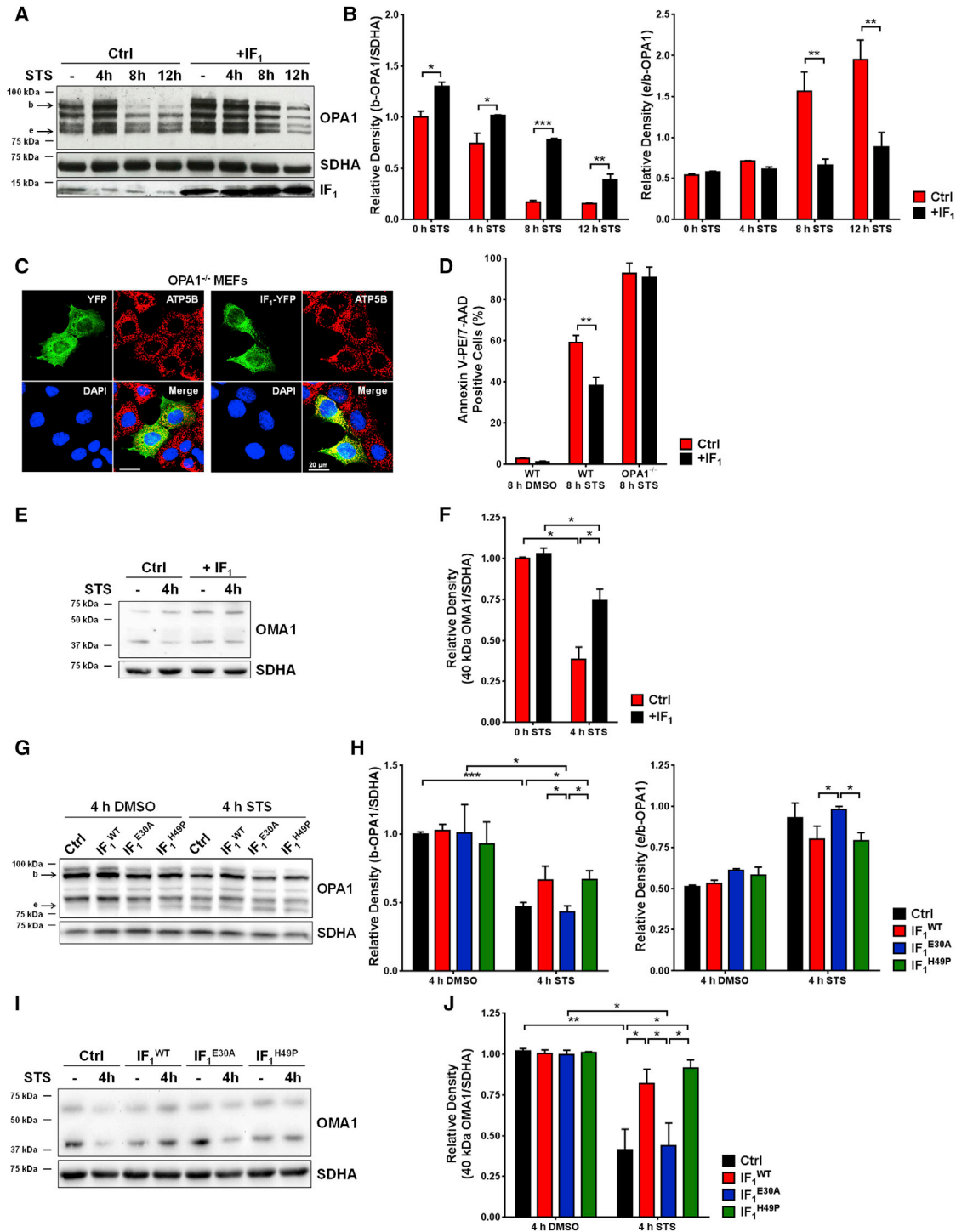
Figure 3. IF$_1$ Impact on Mitochondrial Cristae Structure and Apoptotic Remodeling

(A) Representative western blot of STS-induced cleavage of OPA1 in control and IF$_1$-overexpressing HeLa.

(B) Column diagrams reporting the density of band b (L$_2$-OPA1) and the density ratio between bands e (S$_3$-OPA1) and b at different time points of STS treatment. Data are presented as mean ± SEM; n = 4.

(C) Prototypical fluorescent immunocytochemistry (ICC) images of OPA1$^{-/-}$ MEFs transfected with either YFP or IF$_1$-YFP and immunostained for ATP5B to visualize the mitochondrial network (red). Nuclei were stained with DAPI.

(legend continued on next page)

Changes in mitochondrial mass, such as those induced by expression of WT and mutant IF_1 clones, can directly cause endoplasmic reticulum (ER) stress by affecting the mitochondria-ER coupling and promoting loss of intraluminal Ca^{2+} through alterations in mitochondrial respiration, Ca^{2+} uptake, and reactive oxygen species (ROS) production. For this reason, the Ca^{2+} storing capacity of the ER following transfection with the IF_1 clones was monitored before proceeding through further analysis. The comparable extents of passive Ca^{2+} release induced by inhibiting the sarco-endoplasmic reticulum Ca^{2+} ATPase (SERCA) with thapsigargin ruled out the presence of alterations in the physiological interplay between mitochondria and ER Ca^{2+} signaling (G.G., D.F., and M.C., unpublished data).

The IF_1 mutant clones were finally tested for their capability to counteract apoptosis triggered by staurosporine (STS) (Figure 2L). While WT IF_1 and IF_1^{H49P} were equally effective in reducing the extent of apoptosis independently from activation of the nuclear factor κB (NF-κB) pathway (Figures S4A and S4B), IF_1^{E30A} expression led to sensitization to apoptosis, which was likewise observed in IF_1 KD cells.

IF_1 Prevents Apoptotic Remodeling of Mitochondria by Inhibiting OMA1 Activation and OPA1 Processing

All the data collected so far corroborate previous evidence that the expression level and activity of IF_1 modulate mitochondrial network structure and MIM topology (Campanella et al., 2008; Faccenda et al., 2013b). The anti-apoptotic role of IF_1 does appear to primarily depend on this structural effect, as formerly postulated (Faccenda et al., 2013a).

Therefore, we decided to assess the effect of IF_1 on the apoptotic cleavage of the pro-fusion protein OPA1, which is required for the maintenance of cristae junctions (Frezza et al., 2006). During apoptosis, the stress-induced cleavage of L-OPA1 induces cristae junctions opening and release of pro-apoptotic factors, such as cyt *c*, in the intermembrane space, from where they are subsequently released into the cytosol upon permeabilization of the mitochondrial outer membrane (Scorrano et al., 2002).

STS-induced OPA1 processing was therefore analyzed in control and IF_1-overexpressing HeLa cells, by monitoring apoptosis-dependent loss of L_2-OPA1 (band b) and accumulation of S_3-OPA1 (band e) (Griparic et al., 2007). As shown in Figure 3A, in control cells L_2-OPA1 was almost completely lost after 8 hr of STS incubation. In IF_1-overexpressing cells, instead, it was still retained at 12 hr of STS incubation, and the extent of OPA1 processing was almost halved after 12 hr (Figure 3B). Consistently, loss of IF_1 activity led to increased STS-induced OPA1 processing (Figures S4C and S4D).

To verify whether the presence of OPA1 is necessary for the anti-apoptotic activity of IF_1, we monitored the effect of IF_1 overexpression on mitochondrial morphology and resistance to apoptosis in OPA1-null MEFs (Song et al., 2007). Downregulation of OPA1 induces extensive mitochondrial fragmentation and sensitizes cells to undergo apoptosis (Arnoult et al., 2005). As shown in Figures 3C and 3D, the overexpression of IF_1 was ineffective in rescuing the pro-apoptotic phenotype of OPA1$^{-/-}$ MEFs, suggesting that the structural role of IF_1 on cristae morphology does not overlap with OPA1 activity.

Interestingly, we also observed that increased IF_1 activity counteracts the activation of the MIM-embedded zinc metallopeptidase OMA1. OMA1, activation of which leads to full degradation of L-OPA1, regulates the stress-induced processing of OPA1 (Anand et al., 2014; Jiang et al., 2014). Even though the OMA1-mediated proteolytic cleavage of OPA1is mainly triggered by MIM depolarization (Zhang et al., 2014), the protein is also activated during apoptosis, and knocking down the gene confers a degree of resistance to cell death (Jiang et al., 2014). Therefore, we investigated the proteolytic activity of OMA1 in control and IF_1-overexpressing cells treated with STS (Figure 3E). In both cell types, STS induced a reduction in the levels of the proteolytically active 43-kDa isoform of OMA1, indicating autocatalytic activation of the protein (Baker et al., 2014; Zhang et al., 2014). Nevertheless, this was less pronounced in +IF_1 cells (Figure 3F).

As further proof that IF_1 regulates OMA1-dependent apoptotic processing of OPA1, inactivation of IF_1 by expression of the dominant-negative mutant clone (IF_1^{E30A}) abolished the preservation of OPA1 integrity during apoptosis observed in IF_1-overexpressing cells (Figures 3G and 3H), as well as counteraction of apoptotic OMA1 activation (Figures 3I and 3J).

The OMA1 dependency of the IF_1 protective activity against apoptotic processing of OPA1 was also verified by showing that downregulation of OMA1 completely prevents STS-induced OPA1 cleavage in IF_1-silenced HeLa cells (Figures S4E and S4J).

IF_1 Triggers an ATP-Dependent Antioxidant Pathway that Protects from Apoptotic Damage

A final aspect we took into examination is the impact of IF_1 on the cellular redox status of cancer cells. Reduced IF_1 activity has been linked to increased mitochondrial ROS generation (Campanella et al., 2009; Fujikawa et al., 2012). This event can directly induce the proteolytic cleavage of OPA1 (Baker et al., 2014), a phenomenon that is delayed both in IF_1-overexpressing cells and in presence of the mitochondria-targeted superoxide dismutase (SOD) mimetic MitoTEMPO (Figures S4G and S4H). To clarify whether IF_1 plays an active role in the control of oxidative

(D) Bar chart of the average rate of apoptotic cell death in WT and OPA1$^{-/-}$ MEFs after 8-hr STS treatment. Cells were transfected with either YFP or IF_1-YFP, and stained with annexin V- phycoerythrin (PE) and 7-aminoactinomycin D (7-AAD) to evaluate the percentage of apoptotic dead cells (PE/7-AAD double-positive). Data are presented as mean ± SEM; n = 3 (>200 cells per cover glass).

(E) Western blotting analysis of OMA1 activation in HeLa cells following 4-hr treatment with STS.

(F) Bar chart reporting the STS-induced autocatalytic cleavage of active 40-kDa OMA1 peptide. Data are presented as mean ± SEM; n = 4.

(G) Western blotting analysis of OPA1 isoforms before and after 4-hr treatment with STS in HeLa expressing WT IF_1 or the two mutant clones.

(H) Bar charts of average density of band b and density ratio between bands e and b. Data are presented as mean ± SEM; n = 3.

(I) Representative blot of 60- and 40-kDa OMA1 bands in HeLa cells transfected with WT IF_1, IF_1^{E30A}, or IF_1^{H49P} and treated with 1 μM STS for 4 hr.

(J) Bar chart of average density of the 40-kDa OMA1 band. Data are presented as mean ± SEM; n = 3.
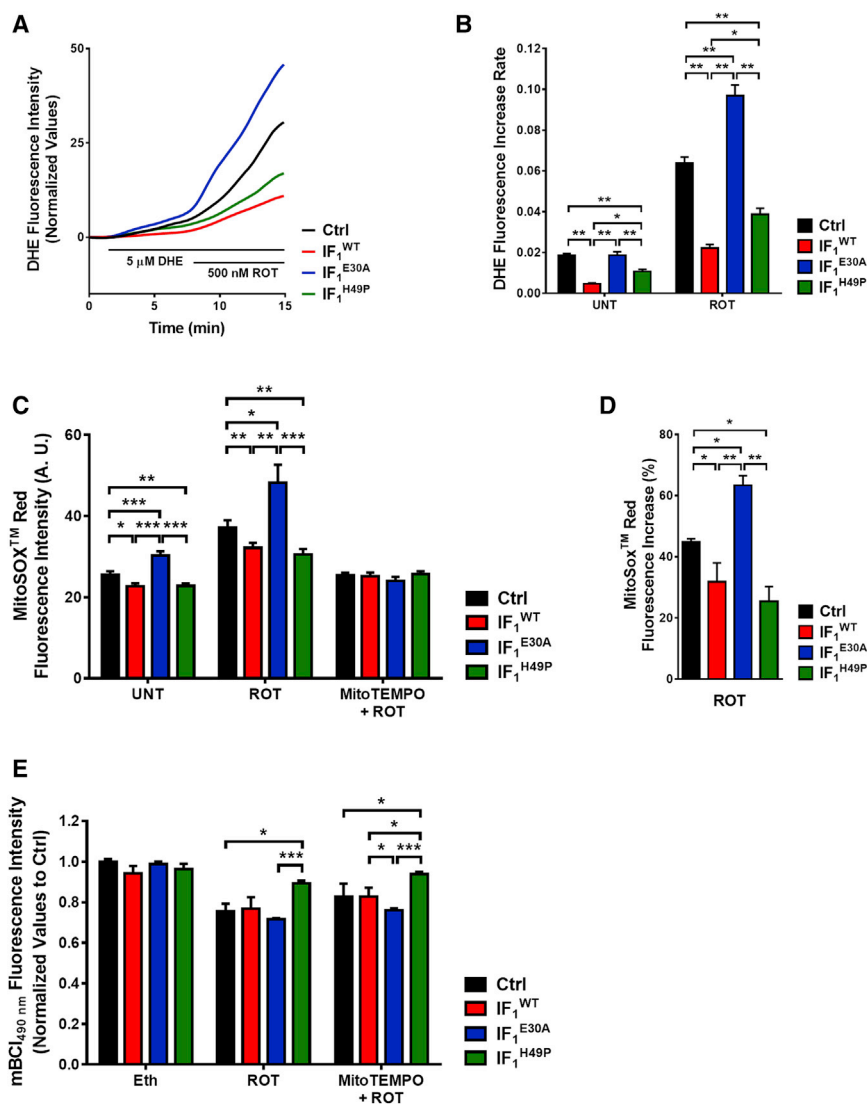
Figure 4. Regulation of Antioxidant Response by IF_1

(A) $O_2 \cdot^-$-dependent increase in DHE emitted fluorescence in HeLa cells expressing IF_1 mutant clones. Cells were co-transfected with YFP and imaged in real time on a confocal microscope in presence of 5 μM DHE, before and after addition of 500 nM ROT.

(B) Bar chart reporting mean slopes of increase in DHE fluorescence intensity, before and after treatment with ROT. Data are presented as mean ± SEM; n = 3 (15–20 cells per cover glass).

(C) Mitochondrial ROS levels in HeLa cells modulated for IF_1 activity measured using MitoSOX Red (5 μM, 10-min incubation). Mitochondrial $O_2 \cdot^-$ generation was elicited by treatment with ROT (500 nM, 45-min incubation). Preincubation with MitoTEMPO was used as a control (20 μM, 45-min incubation). Data are presented as mean ± SEM; n = 4.

(D) Bar chart of percentage of increase in MitoSOX Red fluorescence intensity after treatment with ROT. Data are presented as mean ± SEM.

(E) GSH levels monitored using mBCl (20 μM) in HeLa cells expressing IF_1 mutant clones. The column diagram shows the average mBCl fluorescence intensity after 40-min incubation in untreated cells (45 min Eth, vehicle control), after exposure to ROT (500 nM for 45 min), and in cells pre-incubated with a SOD mimetic (20 μM Mn(III)TMPyP or 20 μM MitoTEMPO for 1 hr) and then treated with ROT (500 nM ROT + 20 μM Mn(III)TMPyP for 45 min or 500 nM ROT + 20 μM MitoTEMPO for 45 min). Data are presented as mean ± SEM; n = 3 (from quadruplicate wells).

stress in cancer cells, cytosolic and mitochondrial superoxide anion ($O_2 \cdot^-$) levels were measured both in basal conditions and upon treatment with ROT, to elicit mitochondrial ROS generation (Figures 4A–4D). Both IF_1 overexpression and the constitutively active mutant clone (IF_1^{H49P}) hindered ROT-induced mitochondrial and cytosolic $O_2 \cdot^-$ accumulation. Disruption of IF_1 inhibitory site (IF_1^{E30A}) led instead to an evident increase in cellular ROS both at steady state and after inhibition of mitochondrial respiration. The mitochondrial origin of ROS was confirmed by preincubation with MitoTEMPO (Figure 4C).

We then measured the levels of reduced GSH in HeLa cells expressing the two IF_1 mutants and treated with ROT. GSH is the prevalent non-protein thiol in cells and plays a key role for the detoxification from H_2O_2 and protein hydroperoxides (Lu, 2009). Interestingly, we observed depletion of GSH levels in all cell types after treatment with ROT (Figure 4E), but this was lower in IF_1^{H49P}-expressing cells. Pre-treatment with MitoTEMPO

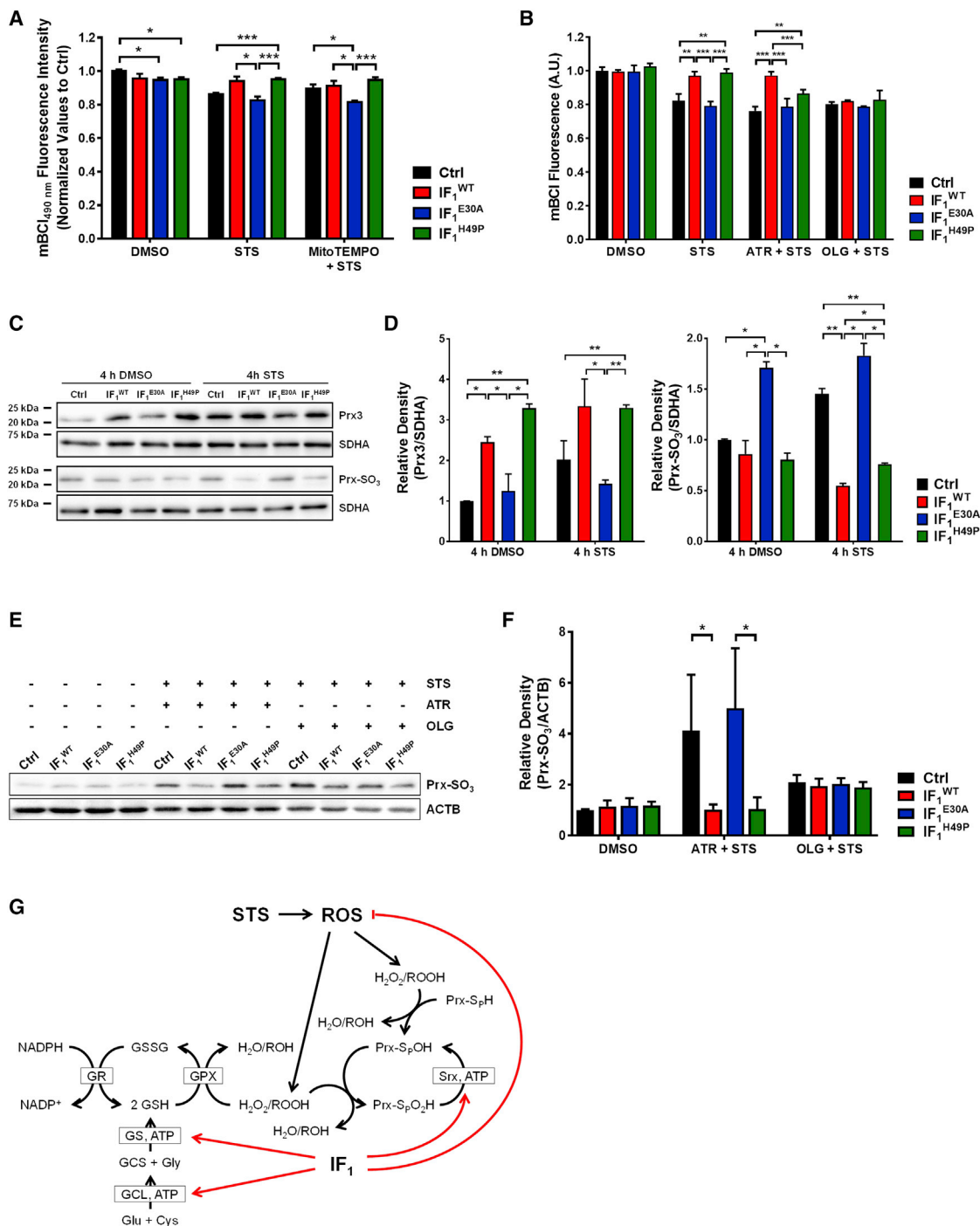reduced the extent of ROT-induced GSH loss, confirming the involvement of mitochondrial ROS.

The effect of STS treatment on the cellular antioxidant defense was then evaluated by monitoring two antioxidant systems, GSH and peroxiredoxins (Prxs). Prxs are a group of cysteine-dependent peroxidases involved in scavenging H_2O_2 and peroxide substrates (Rhee et al., 2005). Depletion of the GSH pool is an early event in apoptosis (Ghibelli et al., 1998), during which it gets extruded and inactivated by oxidation (Hammond et al., 2004; Franco et al., 2007). Along with GSH, mitochondrial Prx3 also regulates cellular response to oxidative stress-induced apoptosis (Chang et al., 2004) and is rapidly oxidized during the process (Cox et al., 2008; Brown et al., 2008).

STS-induced GSH depletion and Prxs hyperoxidation (Prx-SO_3) were therefore evaluated (Figures 5A, 5C, and 5D). The results identify a role for IF_1 in maintenance of the antioxidant capacity of cells during apoptosis. Indeed, differently from IF_1 overexpression, inactivating IF_1 (IF_1^{E30A}) intensified GSH loss and hyperoxidation of the mitochondrial Prx pool during STS-dependent apoptosis. Cells transfected with IF_1^{E30A} also showed increased basal levels of hyperoxidized Prx when compared to cells overexpressing WT IF_1, data that are consistent with the higher ROS

Figure 5. IF₁ Preserves the Cellular Antioxidant Capacity during Apoptotic Stress

(A) Column diagram of mBCl fluorescence intensity in HeLa cells expressing WT IF₁, IF₁^{E30A}, or IF₁^{H49P}. Cells were transfected as in previous mBCl assay and treated with STS (1 μM) for 2 hr or incubated with MitoTEMPO (20 μM for 1 hr) prior to exposure to STS in the presence of the SOD mimetic (1 μM STS + 20 μM MitoTEMPO for 2 hr). To measure steady-state mBCl fluorescent, cells were incubated for 2 hr with DMSO (vehicle control). Data are presented as mean ± SEM; n = 3 (from quadruplicate wells).

(B) STS-induced GSH loss measured via mBCl assay in cells pre-treated with ATR (100 μM, 1 hr) or OLG (2.5 μg/mL, 1 hr). The two compounds were also added during the 2-hr incubation with STS. Data are presented as mean ± SEM; n = 3 (from quadruplicate wells).

(C) Representative western blot of mitochondrial Prx3 and Prx-SO₃; apoptosis-dependent redox inactivation of Prx was induced by treating cells with 1 μM STS for 4 hr.

(D) Column diagram of mean density of Prx3 and Prx-SO₃ protein bands, before and after STS treatment. Data are presented as mean ± SEM; n = 3.

(legend continued on next page)

production observed in these cells. Since both GSH synthesis and re-activation of the hyperoxidized Prxs rely on ATP-dependent reactions (Lu, 2009), maintenance of the cellular antioxidant capacity by IF$_1$ can depend not only on reduction of mitochondrial ROS generation, but also on increased availability of ATP, which is retained in cells overexpressing IF$_1$ after challenge with STS (Figures S4I and S4J). To test this hypothesis, STS-mediated GSH loss and Prx hyperoxidation were also measured in the presence of atractyloside (ATR), to inhibit the mitochondrial import of ADP by blocking the ADP/ATP carrier protein (AAC), or OLG (Figures 5B, 5E, and 5F). The protective effect of IF$_1$ against STS-induced oxidative damage was fully lost in cells co-treated with OLG, confirming that the anti-apoptotic role of IF$_1$ at least partially relies on preservation of intracellular free ATP levels. Interestingly, ATR was instead not effective in preventing the IF$_1$-mediated preservation of GSH and Prx. Since the AAC is the only mitochondrial ADP/ATP translocase (Pebay-Peyroula et al., 2003), the result obtained with ATR may depend on residual high intramitochondrial levels of ATP in cells transfected with WT IF$_1$ or IF$_1^{H49P}$.

As depicted in Figure 5G, IF$_1$ plausibly participates in maintenance of the cellular antioxidant defenses by both decreasing the levels of peroxide substrates and guaranteeing the availability of ATP for preservation of the cellular antioxidant capacity.

DISCUSSION

Numerous studies suggest that IF$_1$ activates pro-survival signaling pathways, induces resistance to cell death, and confers the migratory phenotype in metastatic cancer (Formentini et al., 2012; Faccenda et al., 2013b; Song et al., 2014; Yin et al., 2015). Silencing of IF$_1$ impairs HeLa cells proliferative capacity (Figures 1C and 1D) and blocks the transforming potential of the protein (Figures 1G and 1H and S2C). Interestingly, increased IF$_1$ protein levels and IF$_1$:ATP synthase expression ratio, which characterizes highly metabolic tissues such as brain, heart, and renal proximal tubule (Campanella et al., 2008; Hall et al., 2009; Sánchez-Aragó et al., 2013), was also observed at higher tumor grades (Figures 1A and 1B). On the basis of previous work, we propose that IF$_1$-mediated evasion of cell death relies on preservation of the morphological integrity of mitochondria and prevention of cristae disassembly (Faccenda et al., 2013a). This was therefore examined in greater detail.

Indeed, loss of IF$_1$ causes extensive morphological alteration of the mitochondrial ultrastructure, as originated from a quantitative, in depth analysis of IF$_1$ KD HeLa cells and hepatocytes from IF$_1$ KO mice. We noticed that silencing of IF$_1$ induces formation of abnormally shaped cristae with an arch-like profile (Figure 1E), a phenotype that resembles the one produced by alterations of the supramolecular assembly of the ATP synthase (Habersetzer et al., 2013). This result was somewhat predictable, since there is evidence of IF$_1$ participating in the biogenesis and shaping of mitochondrial cristae by promoting dimerization of the ATP synthase (Minauro-Sanmiguel et al., 2005). The collapse of the organelle during apoptosis also appears to be enhanced (Figure 1F), due to the lower number of lamellar cristae, which facilitates cristae loss and remodeling of the MIM. Furthermore, knocking out IF$_1$ not only causes a reduction in mitochondrial mass, but also induces slight enlargement of the organelle (Figure S2D), reducing the threshold for mitochondrial tolerance to stress-induced swelling.

Considering previous findings and the data reported herein substantiating a role for IF$_1$ in the regulation of mitochondrial morphology during apoptosis, we examined whether the IF$_1$ expression level regulates the apoptotic cleavage of OPA1, which controls formation and maintenance of cristae structure, behaving as anti-apoptotic factor (Varanita et al., 2015). Our results show that IF$_1$ overexpression prevents STS-induced processing of L$_2$-OPA1 (Figures 3A and 3B), therefore limiting cristae remodeling, which is an essential step of mitochondrial commitment to apoptosis (Scorrano et al., 2002).

Recent work has proposed that apoptotic cleavage of OPA1 predominantly depends on stress-triggered activation of OMA1 (Anand et al., 2014; Zhang et al., 2014; Jiang et al., 2014). This event is induced by various cellular stress signals, such as decreased mitochondrial ATP levels, altered $\Delta\Psi_m$ and oxidative stress (Baker et al., 2014; Bohovych et al., 2014; Zhang et al., 2014), all of which often accompany apoptosis progression. In this study, we show that IF$_1$ preserves OPA1 integrity during apoptosis by counteracting the autocatalytic cleavage of OMA1 and, therefore, its proteolytic activity (Figures 3E and 3F). IF$_1$-regulated maintenance of intracellular ATP levels, which is protective against both ischemic/hypoxic and apoptotic damage (Figures 2H and 2K), can represent a potential mechanism for impaired OMA1-mediated processing of OPA1.
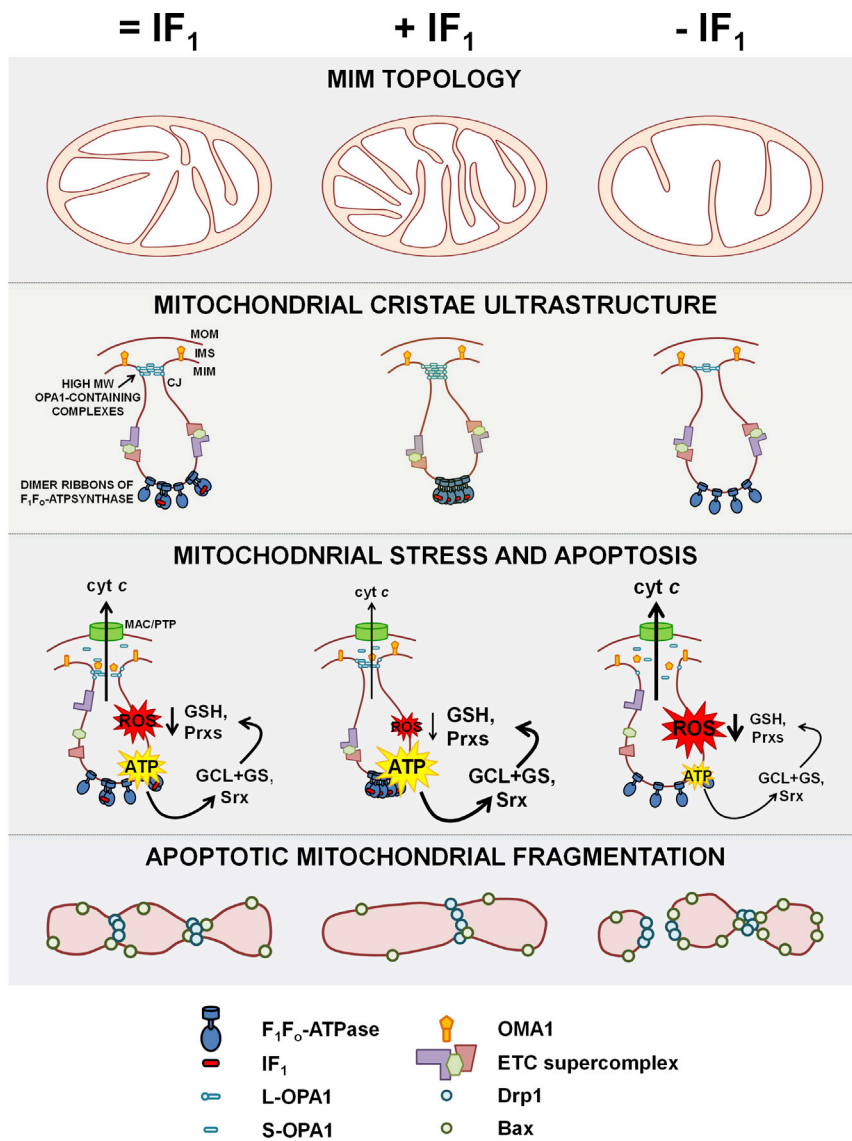
However, an alternative explanatory mechanism for this is linked with the ability of IF$_1$ to activate an ATP-dependent antioxidant pathway, which relies on preservation of GSH and Prx activity and is intimately involved with the anti-apoptotic function of IF$_1$ (Figure 5).

Oxidative stress has long been considered as one of the driving forces in the tumorigenic process (Kensler and Trush, 1984; Burdon et al., 1990). However, increased cellular ROS production must be tightly controlled, in order to avoid excessive cellular damage that can lead to cell death. Due to higher levels of ROS accumulation, cancer cells are closer to the threshold of redox stress in which apoptosis is favored over cell proliferation (Giorgio et al., 2007). The role of IF$_1$ on mitochondrial production of ROS in cancer cells is still debatable. Reduced IF$_1$ activity has been correlated with higher levels of ROS (Campanella et al., 2009; Fujikawa et al., 2012); however, augmented mitochondrial ROS production has also been observed in cancer cells overexpressing IF$_1$ (Formentini et al., 2012) and has been linked to activation of a pro-survival retrograde response. In this study, we evaluated the rate of $O_2^{\bullet-}$ production in HeLa cells transfected with the

(E) Representative blot of cellular Prx hyperoxidation (Prx-SO$_3$) in cells treated with 1 μM STS (4 hr) in the presence of ATR (100 μM) or OLG (2.5 μg/mL). Cells were pre-incubated for 1 hr with the compounds prior to apoptosis induction (DMSO vehicle was used as control).
(F) Bar chart of average Prx-SO$_3$ density in the presence of ATR or OLG. Data are presented as mean ± SEM; n = 3.
(G) Schematic representation of the GSH and Prx antioxidant pathways. Increased levels of IF$_1$ may protect from STS-triggered ROS-damage by lowering mitochondrial ROS production and maintaining sufficient ATP levels for de novo synthesis of GSH and Srx-dependent reactivation of hyperoxidized Prxs.

= IF$_1$ + IF$_1$ - IF$_1$

MIM TOPOLOGY

MITOCHONDRIAL CRISTAE ULTRASTRUCTURE

MOM
IMS
MIM
HIGH MW
OPA1-CONTAINING
COMPLEXES
CJ

DIMER RIBBONS OF
F$_1$F$_o$-ATPSYNTHASE

MITOCHODNRIAL STRESS AND APOPTOSIS

cyt *c*
MAC/PTP
ROS
GSH,
Prxs
ATP
GCL+GS,
Srx

cyt *c*
ROS ↓ GSH,
Prxs
ATP
GCL+GS,
Srx

cyt *c*
ROS ↓ GSH,
Prxs
ATP
GCL+GS,
Srx

APOPTOTIC MITOCHONDRIAL FRAGMENTATION

F$_1$F$_o$-ATPase   OMA1
IF$_1$ ETC supercomplex
L-OPA1   Drp1
S-OPA1   Bax

Figure 6. Working Model for the IF$_1$-Mediated Inhibition of OPA1 Processing and Prxs Inactivation

The cartoon depicts the two stages of mitochondrial commitment to apoptosis and the contribution of IF$_1$ to the oncogenic phenotype. In the left panel, IF$_1$ expression level affects mitochondrial ultrastructure by modulating the rate of ATP synthase dimerization, thereby altering the shape and organization of cristae membranes. In the right panel, inhibition of apoptosis by IF$_1$ is presented. Increased levels of IF$_1$ improve the stability of mitochondrial membranes, limiting both apoptotic mitochondrial remodeling (dependent on the processing of OPA1 by OMA1) and permeabilization (which leads to cyt *c* release). Moreover, the enzymatic efficiency of the ATP synthase is preserved, hindering ROS production and ATP loss. Therefore, cellular antioxidant defenses are conserved, and oxidative stress-induced tumor suppression is counteracted.

In line with this, we observed that the cellular levels of reduced GSH vary accordingly to IF$_1$ activity. Indeed, oxidative depletion of the cellular GSH pool following inhibition of mitochondrial respiration and under STS treatment was less pronounced in IF$_1$-overexpressing cells and in those transfected with the constitutively active clone (Figures 4E and 5A). Moreover, we showed that IF$_1$ has a protective effect toward oxidative inactivation of mitochondrial Prx, thus confirming the antioxidant capacity of IF$_1$ (Figures 5C and 5D). Here, we showed that increased IF$_1$ activity reduces apoptotic inactivation of Prx3 and can therefore protect from ROS-dependent apoptosis.

Considering that GSH synthesis from glutamate and cysteine relies on an ATP-

two IF$_1$ mutant clones upon inhibition of complex I and observed that ROS accumulation is reduced upon overexpression of IF$_1$, while cellular ROS levels are tangibly increased when IF$_1$ activity is compromised, and the ATP synthase reversal is unrestrained (Figures 4A–4D). This might not only be a direct consequence of the variation in the mitochondrial respiratory efficiency caused by changes in IF$_1$ levels (Figures 2B and 2C), but also partially depend on the observed alteration in the mitochondrial network morphology. Overexpression of the protein induces an increase in mitochondrial mass and promotes the elongation and interconnectivity of the network (Figures 2J, 2K, S3G, and S3H), all of which enhance mitochondrial function, thereby lowering the rate of toxic ROS that are generated by inefficient respiration. Indeed, both efficient mitochondrial dynamics and fusion of the network favor mitochondrial respiratory capacity (Picard et al., 2013), while excessive fragmentation is often accompanied by high levels of ROS production (Yu et al., 2006, 2008).

driven, two-step reaction (Lu, 2009), and reactivation of hyperoxidized Prx (Prx-SO$_3$) is catalyzed by the ATP-dependent enzyme sulfiredoxin (Srx) (Rhee et al., 2007), the identified antioxidant activity of IF$_1$ under stress conditions can rely on maintenance of cellular ATP provision (Figures S5C and S5D). Indeed, the protective effect of IF$_1$ against STS-induced GSH and Prx inactivation is lost upon administration of OLG (Figures 5B, 5E, and 5F), a potent inhibitor of the ATP synthase activity, confirming that preservation of ATP synthesis is importantly involved in the antioxidant and anti-apoptotic role of IF$_1$.

Here, we prove that IF$_1$, by targeting ATP dissipation, ultimately protects from excessive oxidative stress (Figure 4G) and ROS-induced cell death. As summarized in Figure 6, this unveils a preferential mechanism for evasion of apoptosis and acquisition of chemoresistance in tumor, via coordination of mitochondrial bioenergetics and dynamics to retain mitochondrial function and membrane integrity.

EXPERIMENTAL PROCEDURES

Cell Culture

HeLa cervical adenocarcinoma cell line and MEFs were obtained from the American Type Culture Collection (ATCC; https://www.atcc.org/). Stable IF_1 knockdown (IF_1^{KD}) and scrambled control (Scrm) HeLa cell lines were prepared as previously described (Fujikawa et al., 2012). IF_1 KO MEFs were prepared from IF_1 KO mice (Nakamura et al., 2013). WT $OPA1^{-/-}$ MEFs (Song et al., 2007) were kindly donated by Prof. Luca Scorrano (University of Padua, Italy). All cell lines were cultured and prepared according to standard mammalian tissue culture protocols (please refer to Supplemental Experimental Procedures for details). All animal experiments were carried out according to the correct institutional procedures.

Transfection and Gene Expression

Upregulation of IF_1 was achieved by using the full-length ORF cDNA clone of human ATPase inhibitory factor 1 (ATPIF1), transcript variant 1, mRNA (321 bp; GenBank accession number: NM_016311.4), which was subcloned into the MCS of the plasmidial vector pCMV-Sport6. The fluorescent-tagged version of IF_1 was obtained by subcloning of (cDNA) ATPIF1 into the MCS of the plasmidial vector pEYFP-N1, which was carried out by Mutagenex. IF_1 mutant clones (IF_1^{E30A} and IF_1^{H49P}) were obtained from Mutagenex through site-directed mutagenesis and subcloning of the mutated cDNAs into pEYFP-N1. The untagged versions of the mutant clones were obtained by subsequent deletion of the yellow fluorescent protein (YFP) coding sequence, which was equally realized by Mutagenex.

Depletion of IF_1 and OMA1 expression in HeLa cells was instead achieved by RNA interference technique, using the following mRNA-specific predesigned small interfering RNAs (siRNAs): human IF_1 (Hs_ATPIF1_2 FlexiTube siRNA) (QIAGEN, SI00308112) and human OMA1 (esiRNA1) (Sigma-Aldrich, Mission esiRNA EHU072451).

Transfection with the appropriate cDNA or siRNA was carried out 36–48 hr prior to experimentation using the calcium phosphate method. HeLa were transfected when 50%–60% confluent, while MEFs at 30%–40% confluence.

Fluorescence Immunohistochemistry Analysis of Breast Cancer TMAs

Slides were deparaffinized in xylene, rehydrated, and incubated in citrate buffer for heat-induced epitope retrieval. After cell permeabilization in 0.025% Triton X-100 in Tris-buffered saline (TBS), slides were incubated with blocking solution (10% normal goat serum [NGS], 1% BSA in TBS) for 2 hr at room temperature (RT). Overnight incubation at 4°C with α-IF1 and α-ATP5B primary antibodies was followed by 1-hr treatment at RT in the dark with the appropriate fluorescently labeled secondary antibodies (see Supplemental Experimental Procedures). All antibodies were diluted in TBS supplemented with 1% BSA. Nuclear staining was carried out with DAPI. Images were acquired using a Leica DM IRB inverted fluorescence microscope. Analysis was conducted with Volocity and heatmaps prepared on ImageJ.

Soft Agar Colony Formation Assay

6-well plates were filled with 1.5 mL of 0.6% low melting point agarose in DMEM supplemented with 5% fetal bovine serum (FBS) as a bottom layer. Control and IF_1 KD HeLa cells, suspended in 0.6% agarose, were plated on the upper layer of soft agar (5,000 cells/well). Viable colonies (>100 μm) were manually counted in nine random areas per well under a microscope.

Analysis of Mitochondrial Inner Structure

After 4 hr STS treatment, control and IF_1 KD HeLa (grown on cover glasses) were immediately fixed and processed for transmission electron microscopy (please refer to Supplemental Experimental Procedures). Images were acquired using a JEOL JEM-1010 transmission electron microscope. Analysis of cristae density was done in ImageJ and reported as number of cristae per unit of mitochondrial area (the total number of cristae was divided by the entire mitochondrial cross sectional area).

Xenograft Tumor Analysis

All xenograft procedures were conducted according to the correct institutional procedures (approved by Kyoto Sangyo University). MEF cell lines were estab-

lished from WT and IF_1 KO mouse embryos (Nakamura et al., 2013) and then transformed by retroviral infection of H-Ras^{V12}. Cell growth of transformed IF_1 KO MEFs was confirmed to be equal to that of the WT counterpart, as shown in Figure S1B. 1×10^7 immortalized MEF cells in 100 μL of PBS were grafted to right (WT) and left (IF_1 KO) side of six nude mice. After 20 days, growth of tumor of nude mice was recorded.

Determination of Cellular OCR

On the day before experiment, HeLa cells, transfected with an empty plasmid (as control) or with one IF_1 construct (WT IF_1, IF_1^{E30A}, IF_1^{H49P}), were seeded in triplicate on Seahorse XFp cell-culture miniplates (3×10^4 cells per well). OCR was measured with a Seahorse XFp extracellular flux analyzer, using a Seahorse XFp cell mito stress test kit and following manufacturer's instructions (as reported in Supplemental Experimental Procedures).

Data obtained from the assay were analyzed with the Seahorse XFp analysis software and normalized to the amount of mitochondrial protein of each sample, in order to avoid misinterpretation of data due to differences in mitochondrial mass between samples (as explained in Supplemental Experimental Procedures).

Live-Cell Luciferase Assay

The comparison of basal levels of free cytosolic and mitochondrial ATP was achieved by using targeted luciferase constructs.

HeLa cells were co-transfected with cytosol- or mitochondria-targeted luciferase (cLuc or mLuc) and IF_1, IF_1^{E30A}, IF_1^{H49P}, or an empty plasmid (as control). After 36–48 hr from transfection, cells were transferred into the thermostatted perfusion chamber of a custom built luminometer, and photon emission was measured before and after addition of 20 mM D-luciferin. Once the ATP-dependent luminescent signal had reached a plateau, 2.5 μg/mL OLG was added to evaluate the contribution of the ATP synthase to cytosolic and mitochondrial ATP levels.

Measurement of $\Delta\Psi_m$

Continuous monitoring of NaCN-induced mitochondrial depolarization was achieved by loading cells with the fluorescent potentiometric dye tetramethyl rodamine methyl ester (TMRM).

Cells were co-transfected with YFP and WT IF_1, IF_1^{E30A}, or IF_1^{H49P} (an empty plasmid was used as control) and loaded with 30 nM TMRM prior to experiment. Cells were imaged using a Nikon Eclipse Ti-E inverted fluorescence microscope, and mitochondrial TMRM fluorescence decay was monitored in real-time after administration of 1 mM NaCN until a plateau. Directional dye behavior was confirmed by adding FCCP (20 nM). Settings were kept constant between experiments. Time series were analyzed using Andor iQ2.

Measurement of Cellular ATP Depletion

[ATP]$_i$ was indirectly measured by using UV-excitable Mag-Fura-2, AM (please refer to Supplemental Experimental Procedures). Cells were transfected as for TMRM analysis and, before imaging, incubated with 5 μM Mag-Fura-2. Experiments were conducted in glucose-free medium (GFM), and ATP depletion was induced by adding iodoacetic acid (IAA; 2 mM) and NaCN (1 mM). Time series were acquired using a Nikon Eclipse Ti-E inverted fluorescence microscope, and changes in Mag-Fura-2$_{340/380\ nm}$ emission intensity ratio was then recorded until a plateau. Settings were kept constant between experiments. Images were processed and analyzed using Andor iQ2. Line slopes were calculated through data linearization and fitting (linear interpolation).

Evaluation of Cell Death and Apoptosis Rates

The rate of cell death in ischemic-like conditions was measured with combined propidium iodide (PI)-DAPI nuclear stain (CPD). HeLa cells grown on 6-well plates were co-transfected with YFP and either one of the IF_1 constructs (WT IF_1, IF_1^{E30A}, or IF_1^{H49P}) or an empty plasmid (as control). 2-hr incubation in ischemic buffer (GFM supplemented with 1 mM NaCN and 2 mM IAA) was carried out 36–48 hr after transfection. CPD procedure was performed directly after treatment (see Supplemental Experimental Procedures). Identification of apoptotic cells was carried out with either terminal deoxynucleotidyl transferase (TdT) dUTP nick-end labeling (TUNEL) assay or annexin V-phycoerythrin (PE) and 7-aminoactinomycin D (7-AAD) double stain, using a Leica

DM IRB inverted fluorescence microscope (see Supplemental Experimental Procedures).

Analysis of Mitochondrial Morphology

Fluorescent immunocytochemistry (ICC) analysis of the mitochondrial network in OPA1$^{-/-}$ MEFs was carried out after transfection with either IF$_1$-YFP or YFP (as control). Cells were fixed in 4% paraformaldehyde (PFA) in PBS and permeabilized in 0.1% Triton X-100. Blocking was carried out for 1 hr at RT in 10% NGS, 3% BSA, and 0.01% Triton X-100 in PBS. Cells were then incubated overnight with α-ATP5B antibody at 4°C in blocking solution in a humidified chamber and for 1 hr at RT with the appropriate fluorescently tagged secondary antibody. 300 nM DAPI in PBS was used for nuclear staining (10 min at RT in the dark).

Mitochondrial profile area was assessed in cells transfected with either one of the YFP-tagged IF$_1$ constructs (IF$_1^{WT}$-YFP, IF$_1^{E30A}$-YFP, IF$_1^{H49P}$-YFP) or YFP (as control), by using MitoTracker Red FM (50 nM). z stacks of transfected cells were obtained using a Zeiss LSM 510 confocal laser scanning microscope (CLSM). The number of slices and step size were kept constant, and the microscope detection settings were fixed. The mitochondrial profile area (% of cytosolic volume occupied by mitochondria) was calculated with Volocity.

The shape descriptors aspect ratio (AR) and form factor (FF) were also evaluated as measures of mitochondrial elongation and branching, respectively. Cells, co-transfected with mitochondria-targeted green fluorescent protein (mtGFP), were imaged using a Leica TCS SP5 CLSM. z stacks were acquired as described above. Image analysis and calculation of shape descriptors was done in ImageJ.

Sample Protein Preparation and Western Blot Analysis

Cells were grown on 10-cm plates in order to reach 80%–85% confluence before treatment and lysis.

Chemical cross-linking for studying IF$_1$ oligomerization was carried out prior to cell lysis with the lipid-soluble cross-linker 1,5-difluoro-2,4-dinitrobenzene (DFDNB). Protocols are reported in Supplemental Experimental Procedures.

Protein concentration was quantified using a BCA protein assay kit. Equal amounts of protein (20 μg) were resolved on SDS-PAGE gels and transferred to nitrocellulose membranes. After blocking, the membranes were incubated overnight at 4°C with the appropriate primary antibody and then for 1 hr at RT with the corresponding peroxidase-conjugated secondary antibody (all antibodies are listed in Supplemental Experimental Procedures). Immunoreactive bands were analyzed with ImageJ software.

Measurement of O$_2$$\cdot^-$ Levels

Cytosolic O$_2$$\cdot^-$ levels were measured with dihydroethidium (DHE). Cells were co-transfected with YFP and WT IF$_1$, IF$_1^{E30A}$, IF$_1^{H49P}$ or an empty plasmid (as control) and imaged using a Zeiss LSM 510 CLSM confocal microscope. 5 μM DHE was added, and its fluorescence increase was recorded for approximately 10 min before challenge with 500 nM ROT (ROT). The same settings were used in all experiments, and the slopes of the generated curves were calculated through linear regression.

Analysis of ROT-induced mitochondrial ROS production was performed with MitoSOX Red (5 μM), by comparing the intensity of its fluorescent signal within mitochondria in untreated and ROT-treated cells.

Determination of Cellular GSH Levels with Monochlorobimane

Monochlorobimane (mBCl) assay was performed using a 96-well plate and a Tecan Infinite M200 PRO microplate reader.

Cells were co-transfected with YFP cDNA and WT IF$_1$, IF$_1^{E30A}$, or IF$_1^{E30A}$ (an empty plasmid was used as control). Before experiment, cells were trypsinized, counted, and resuspended in recording medium (RM) at a standard concentration of 1×10^6 cells/mL. 1×10^5 cells were then added in octuplicate wells. 20 μM mBCl was then concomitantly added to all sample wells with a multichannel pipette, and the plate was inserted into the microplate reader, setting constant temperature of 37°C and 5% CO$_2$. The mBCl emitted fluorescence intensity was measured every 10 min over a 40-min period.

Measurement of Mitochondrial ATP Depletion

[ATP]$_m$ was measured via a luciferin-luciferase assay. HeLa cells were co-transfected with IF$_1$ (or an empty plasmid as control) and mLuc. Cells were first perfused with RM supplemented with 100 μM luciferin, and proton counting was carried out with a custom-built luminometer. Following stabilization of the luminescent signal, cells were continuously exposed to luciferin (100 μM) and STS (1 μM).

Statistical Analysis

Statistical analyses were performed using Prism 6. Data are presented as mean ± SEM. Variations between three or more independent groups were determined using one-way ANOVA. In case of rejection of the null hypothesis, determination of which groups differ from each other (post hoc test) was completed using the Tukey's honest significant difference (HSD) test. A p value of less than 0.05 was considered significant (*p < 0.05; **p < 0.01; ***p < 0.001).

SUPPLEMENTAL INFORMATION

Supplemental Information includes Supplemental Experimental Procedures and four figures and can be found with this article online at http://dx.doi.org/10.1016/j.celrep.2017.01.070.

REFERENCES

Anand, R., Wai, T., Baker, M.J., Kladt, N., Schauss, A.C., Rugarli, E., and Langer, T. (2014). The i-AAA protease YME1L and OMA1 cleave OPA1 to balance mitochondrial fusion and fission. J. Cell Biol. *204*, 919–929.

Arnoult, D., Grodet, A., Lee, Y.J., Estaquier, J., and Blackstone, C. (2005). Release of OPA1 during apoptosis participates in the rapid and complete release of cytochrome c and subsequent mitochondrial fragmentation. J. Biol. Chem. *280*, 35742–35750.

Baker, M.J., Lampe, P.A., Stojanovski, D., Korwitz, A., Anand, R., Tatsuta, T., and Langer, T. (2014). Stress-induced OMA1 activation and autocatalytic turnover regulate OPA1-dependent mitochondrial dynamics. EMBO J. *33*, 578–593.

Barbato, S., Sgarbi, G., Gorini, G., Baracca, A., and Solaini, G. (2015). The inhibitor protein (IF1) of the F1F0-ATPase modulates human osteosarcoma cell bioenergetics. J. Biol. Chem. *290*, 6338–6348.

Bason, J.V., Runswick, M.J., Fearnley, I.M., and Walker, J.E. (2011). Binding of the inhibitor protein IF(1) to bovine F(1)-ATPase. J. Mol. Biol. *406*, 443–453.

Benard, G., and Rossignol, R. (2008). Ultrastructure of the mitochondrion and its bearing on function and bioenergetics. Antioxid. Redox Signal. *10*, 1313–1342.

Bohovych, I., Donaldson, G., Christianson, S., Zahayko, N., and Khalimonchuk, O. (2014). Stress-triggered activation of the metalloprotease Oma1 involves its C-terminal region and is important for mitochondrial stress protection in yeast. J. Biol. Chem. *289*, 13259–13272.

Brown, K.K., Eriksson, S.E., Arnér, E.S., and Hampton, M.B. (2008). Mitochondrial peroxiredoxin 3 is rapidly oxidized in cells treated with isothiocyanates. Free Radic. Biol. Med. *45*, 494–502.

Burdon, R.H., Gill, V., and Rice-Evans, C. (1990). Oxidative stress and tumour cell proliferation. Free Radic. Res. Commun. *11*, 65–76.

Buzhynskyy, N., Sens, P., Prima, V., Sturgis, J.N., and Scheuring, S. (2007). Rows of ATP synthase dimers in native mitochondrial inner membranes. Biophys. J. *93*, 2870–2876.

Cabezon, E., Butler, P.J., Runswick, M.J., and Walker, J.E. (2000). Modulation of the oligomerization state of the bovine F1-ATPase inhibitor protein, IF1, by pH. J. Biol. Chem. *275*, 25460–25464.

Campanella, M., Casswell, E., Chong, S., Farah, Z., Wieckowski, M.R., Abramov, A.Y., Tinker, A., and Duchen, M.R. (2008). Regulation of mitochondrial structure and function by the F1Fo-ATPase inhibitor protein, IF1. Cell Metab. *8*, 13–25.

Campanella, M., Seraphim, A., Abeti, R., Casswell, E., Echave, P., and Duchen, M.R. (2009). IF1, the endogenous regulator of the F(1)F(o)-ATPsynthase, defines mitochondrial volume fraction in HeLa cells by regulating autophagy. Biochim. Biophys. Acta *1787*, 393–401.

Chang, T.S., Cho, C.S., Park, S., Yu, S., Kang, S.W., and Rhee, S.G. (2004). Peroxiredoxin III, a mitochondrion-specific peroxidase, regulates apoptotic signaling by mitochondria. J. Biol. Chem. *279*, 41975–41984.

Cox, A.G., Pullar, J.M., Hughes, G., Ledgerwood, E.C., and Hampton, M.B. (2008). Oxidation of mitochondrial peroxiredoxin 3 during the initiation of receptor-mediated apoptosis. Free Radic. Biol. Med. *44*, 1001–1009.

Cunniff, B., Wozniak, A.N., Sweeney, P., DeCosta, K., and Heintz, N.H. (2014). Peroxiredoxin 3 levels regulate a mitochondrial redox setpoint in malignant mesothelioma cells. Redox Biol. *3*, 79–87.

Daum, B., Walter, A., Horst, A., Osiewacz, H.D., and Kühlbrandt, W. (2013). Age-dependent dissociation of ATP synthase dimers and loss of inner-membrane cristae in mitochondria. Proc. Natl. Acad. Sci. USA *110*, 15301–15306.

Davies, K.M., Anselmi, C., Wittig, I., Faraldo-Gómez, J.D., and Kühlbrandt, W. (2012). Structure of the yeast F1Fo-ATP synthase dimer and its role in shaping the mitochondrial cristae. Proc. Natl. Acad. Sci. USA *109*, 13602–13607.

Faccenda, D., Tan, C.H., Duchen, M.R., and Campanella, M. (2013a). Mitochondrial IF$_1$ preserves cristae structure to limit apoptotic cell death signaling. Cell Cycle *12*, 2530–2532.

Faccenda, D., Tan, C.H., Seraphim, A., Duchen, M.R., and Campanella, M. (2013b). IF1 limits the apoptotic-signalling cascade by preventing mitochondrial remodelling. Cell Death Differ. *20*, 686–697.

Formentini, L., Sánchez-Aragó, M., Sánchez-Cenizo, L., and Cuezva, J.M. (2012). The mitochondrial ATPase inhibitory factor 1 triggers a ROS-mediated retrograde prosurvival and proliferative response. Mol. Cell *45*, 731–742.

Franco, R., Panayiotidis, M.I., and Cidlowski, J.A. (2007). Glutathione depletion is necessary for apoptosis in lymphoid cells independent of reactive oxygen species formation. J. Biol. Chem. *282*, 30452–30465.

Frank, S., Gaume, B., Bergmann-Leitner, E.S., Leitner, W.W., Robert, E.G., Catez, F., Smith, C.L., and Youle, R.J. (2001). The role of dynamin-related protein 1, a mediator of mitochondrial fission, in apoptosis. Dev. Cell *1*, 515–525.

Frezza, C., Cipolat, S., Martins de Brito, O., Micaroni, M., Beznoussenko, G.V., Rudka, T., Bartoli, D., Polishuck, R.S., Danial, N.N., De Strooper, B., and Scorrano, L. (2006). OPA1 controls apoptotic cristae remodeling independently from mitochondrial fusion. Cell *126*, 177–189.

Fujikawa, M., Imamura, H., Nakamura, J., and Yoshida, M. (2012). Assessing actual contribution of IF1, inhibitor of mitochondrial FoF1, to ATP homeostasis,

cell growth, mitochondrial morphology, and cell viability. J. Biol. Chem. *287*, 18781–18787.

Galluzzi, L., Bravo-San Pedro, J.M., Vitale, I., Aaronson, S.A., Abrams, J.M., Adam, D., Alnemri, E.S., Altucci, L., Andrews, D., Annicchiarico-Petruzzelli, M., et al. (2015). Essential versus accessory aspects of cell death: Recommendations of the NCCD 2015. Cell Death Differ. *22*, 58–73.

García, J.J., Morales-Ríos, E., Cortés-Hernandez, P., and Rodríguez-Zavala, J.S. (2006). The inhibitor protein (IF1) promotes dimerization of the mitochondrial F1F0-ATP synthase. Biochemistry *45*, 12695–12703.

Ghibelli, L., Fanelli, C., Rotilio, G., Lafavia, E., Coppola, S., Colussi, C., Civitareale, P., and Ciriolo, M.R. (1998). Rescue of cells from apoptosis by inhibition of active GSH extrusion. FASEB J. *12*, 479–486.

Giorgio, M., Trinei, M., Migliaccio, E., and Pelicci, P.G. (2007). Hydrogen peroxide: A metabolic by-product or a common mediator of ageing signals? Nat. Rev. Mol. Cell Biol. *8*, 722–728.

Griparic, L., Kanazawa, T., and van der Bliek, A.M. (2007). Regulation of the mitochondrial dynamin-like protein Opa1 by proteolytic cleavage. J. Cell Biol. *178*, 757–764.

Habersetzer, J., Larrieu, I., Priault, M., Salin, B., Rossignol, R., Brèthes, D., and Paumard, P. (2013). Human F1F0 ATP synthase, mitochondrial ultrastructure and OXPHOS impairment: A (super-)complex matter? PLoS ONE *8*, e75429.

Hall, A.M., Unwin, R.J., Parker, N., and Duchen, M.R. (2009). Multiphoton imaging reveals differences in mitochondrial function between nephron segments. J. Am. Soc. Nephrol. *20*, 1293–1302.

Hammond, C.L., Madejczyk, M.S., and Ballatori, N. (2004). Activation of plasma membrane reduced glutathione transport in death receptor apoptosis of HepG2 cells. Toxicol. Appl. Pharmacol. *195*, 12–22.

Hanahan, D., and Weinberg, R.A. (2011). Hallmarks of cancer: The next generation. Cell *144*, 646–674.

Jiang, X., Jiang, H., Shen, Z., and Wang, X. (2014). Activation of mitochondrial protease OMA1 by Bax and Bak promotes cytochrome c release during apoptosis. Proc. Natl. Acad. Sci. USA *111*, 14782–14787.

Kensler, T.W., and Trush, M.A. (1984). Role of oxygen radicals in tumor promotion. Environ. Mutagen. *6*, 593–616.

Lu, S.C. (2009). Regulation of glutathione synthesis. Mol. Aspects Med. *30*, 42–59.

Martinou, J.C., and Youle, R.J. (2011). Mitochondria in apoptosis: Bcl-2 family members and mitochondrial dynamics. Dev. Cell *21*, 92–101.

Matic, I., Cocco, S., Ferraina, C., Martin-Jimenez, R., Florenzano, F., Crosby, J., Lupi, R., Amadoro, G., Russell, C., Pignataro, G., et al. (2016). Neuroprotective coordination of cell mitophagy by the ATPase Inhibitory Factor 1. Pharmacol. Res. *103*, 56–68.

Minauro-Sanmiguel, F., Wilkens, S., and García, J.J. (2005). Structure of dimeric mitochondrial ATP synthase: Novel F0 bridging features and the structural basis of mitochondrial cristae biogenesis. Proc. Natl. Acad. Sci. USA *102*, 12356–12358.

Nakamura, J., Fujikawa, M., and Yoshida, M. (2013). IF1, a natural inhibitor of mitochondrial ATP synthase, is not essential for the normal growth and breeding of mice. Biosci. Rep. *33*, Published online September 17, 2013.

Ni, H.M., Williams, J.A., and Ding, W.X. (2015). Mitochondrial dynamics and mitochondrial quality control. Redox Biol. *4*, 6–13.

Otera, H., and Mihara, K. (2012). Mitochondrial dynamics: Functional link with apoptosis. Int. J. Cell Biol. *2012*, 821676.

Pebay-Peyroula, E., Dahout-Gonzalez, C., Kahn, R., Trézéguet, V., Lauquin, G.J., and Brandolin, G. (2003). Structure of mitochondrial ADP/ATP carrier in complex with carboxyatractyloside. Nature *426*, 39–44.

Picard, M., Shirihai, O.S., Gentil, B.J., and Burelle, Y. (2013). Mitochondrial morphology transitions and functions: Implications for retrograde signaling? Am. J. Physiol. Regul. Integr. Comp. Physiol. *304*, R393–R406.

Rhee, S.G., Chae, H.Z., and Kim, K. (2005). Peroxiredoxins: A historical overview and speculative preview of novel mechanisms and emerging concepts in cell signaling. Free Radic. Biol. Med. *38*, 1543–1552.

Rhee, S.G., Jeong, W., Chang, T.S., and Woo, H.A. (2007). Sulfiredoxin, the cysteine sulfinic acid reductase specific to 2-Cys peroxiredoxin: Its discovery, mechanism of action, and biological significance. Kidney Int. Suppl. (*106, Suppl*), S3–S8.

Rouslin, W., and Broge, C.W. (1996). IF1 function in situ in uncoupler-challenged ischemic rabbit, rat, and pigeon hearts. J. Biol. Chem. *271*, 23638–23641.

Sánchez-Aragó, M., Formentini, L., García-Bermúdez, J., and Cuezva, J.M. (2012). IF1 reprograms energy metabolism and signals the oncogenic phenotype in cancer. Cell Cycle *11*, 2963–2964.

Sánchez-Aragó, M., Formentini, L., Martínez-Reyes, I., García-Bermudez, J., Santacatterina, F., Sánchez-Cenizo, L., Willers, I.M., Aldea, M., Nájera, L., Juarránz, A., et al. (2013). Expression, regulation and clinical relevance of the ATPase inhibitory factor 1 in human cancers. Oncogenesis *2*, e46.

Sánchez-Cenizo, L., Formentini, L., Aldea, M., Ortega, A.D., García-Huerta, P., Sánchez-Aragó, M., and Cuezva, J.M. (2010). Up-regulation of the ATPase inhibitory factor 1 (IF1) of the mitochondrial H+-ATP synthase in human tumors mediates the metabolic shift of cancer cells to a Warburg phenotype. J. Biol. Chem. *285*, 25308–25313.

Scorrano, L., Ashiya, M., Buttle, K., Weiler, S., Oakes, S.A., Mannella, C.A., and Korsmeyer, S.J. (2002). A distinct pathway remodels mitochondrial cristae and mobilizes cytochrome c during apoptosis. Dev. Cell *2*, 55–67.

Seyfried, T.N., Flores, R.E., Poff, A.M., and D'Agostino, D.P. (2014). Cancer as a metabolic disease: Implications for novel therapeutics. Carcinogenesis *35*, 515–527.

Song, Z., Chen, H., Fiket, M., Alexander, C., and Chan, D.C. (2007). OPA1 processing controls mitochondrial fusion and is regulated by mRNA splicing, membrane potential, and Yme1L. J. Cell Biol. *178*, 749–755.

Song, R., Song, H., Liang, Y., Yin, D., Zhang, H., Zheng, T., Wang, J., Lu, Z., Song, X., Pei, T., et al. (2014). Reciprocal activation between ATPase inhibitory factor 1 and NF-κB drives hepatocellular carcinoma angiogenesis and metastasis. Hepatology *60*, 1659–1673.

Song, I.S., Jeong, Y.J., Jeong, S.H., Heo, H.J., Kim, H.K., Bae, K.B., Park, Y.H., Kim, S.U., Kim, J.M., Kim, N., et al. (2015). FOXM1-induced prx3 regulates stemness and survival of colon cancer cells via maintenance of mitochondrial function. Gastroenterology *149*, 1006–1016.

Tait, S.W., and Green, D.R. (2010). Mitochondria and cell death: Outer membrane permeabilization and beyond. Nat. Rev. Mol. Cell Biol. *11*, 621–632.

Tomasetig, L., Di Pancrazio, F., Harris, D.A., Mavelli, I., and Lippe, G. (2002). Dimerization of F0F1ATP synthase from bovine heart is independent from the binding of the inhibitor protein IF1. Biochim. Biophys. Acta *1556*, 133–141.

Twig, G., and Shirihai, O.S. (2011). The interplay between mitochondrial dynamics and mitophagy. Antioxid. Redox Signal. *14*, 1939–1951.

Varanita, T., Soriano, M.E., Romanello, V., Zaglia, T., Quintana-Cabrera, R., Semenzato, M., Menabò, R., Costa, V., Civiletto, G., Pesce, P., et al. (2015). The OPA1-dependent mitochondrial cristae remodeling pathway controls atrophic, apoptotic, and ischemic tissue damage. Cell Metab. *21*, 834–844.

Vogelstein, B., and Kinzler, K.W. (1993). The multistep nature of cancer. Trends Genet. *9*, 138–141.

Westermann, B. (2012). Bioenergetic role of mitochondrial fusion and fission. Biochim. Biophys. Acta *1817*, 1833–1838.

Wu, J., Shan, Q., Li, P., Wu, Y., Xie, J., and Wang, X. (2015). ATPase inhibitory factor 1 is a potential prognostic marker for the migration and invasion of glioma. Oncol. Lett. *10*, 2075–2080.

Yin, T., Lu, L., Xiong, Z., Wei, S., and Cui, D. (2015). ATPase inhibitory factor 1 is a prognostic marker and contributes to proliferation and invasion of human gastric cancer cells. Biomed. Pharmacother. *70*, 90–96.

Yu, T., Robotham, J.L., and Yoon, Y. (2006). Increased production of reactive oxygen species in hyperglycemic conditions requires dynamic change of mitochondrial morphology. Proc. Natl. Acad. Sci. USA *103*, 2653–2658.

Yu, T., Sheu, S.S., Robotham, J.L., and Yoon, Y. (2008). Mitochondrial fission mediates high glucose-induced cell death through elevated production of reactive oxygen species. Cardiovasc. Res. *79*, 341–351.

Zhang, K., Li, H., and Song, Z. (2014). Membrane depolarization activates the mitochondrial protease OMA1 by stimulating self-cleavage. EMBO Rep. *15*, 576–585.